Supplementary Information for

Balancing electrical and optical losses for efficient Si-perovskite 4-terminal solar cells with solution processed percolation electrodes.

César Omar Ramírez Quiroz[*1], *Yilei Shen* [1], *Michael Salvador* [1, 2], *Karen Forberich* [1], *Nadine Schrenker* [3], *George D. Spyropoulos* [1], *Thomas Heumüller* [1], *Benjamin Wilkinson* [4], *Thomas Kirchartz* [5, 6], *Erdmann Spiecker* [3], *Pierre J. Verlinden* [7], *Xueling Zhang* [7], *Martin A. Green* [4], *Anita Ho-Baillie* [4], *and Christoph J. Brabec* [*1, 8]

[1] *Friedrich-Alexander University Erlangen-Nuremberg, Institute of Materials for Electronics and Energy Technology (I-MEET), Department of Materials Science and Engineering, Erlangen, Germany*

[2] *Kaust Solar Center, King Abdullah University of Science and Technology (KAUST)*

[3] *Center for Nanoanalysis and Electron Microscopy (CENEM), Department Werkstoffwissenschaften, Friedrich-Alexander University Erlangen-Nuremberg, Cauerstraße 6, 91058 Erlangen, Germany.*

[4] *The Australian Centre for Advanced Photovoltaics (ACAP), School of Photovoltaic and Renewable Energy Engineering, University of New South Wales, Sydney 2052, Australia.*

[5] *IEK-5 Photovoltaik, Forschungszentrum Jülich GmbH, 52428 Jülich, Germany.*

[6] *Faculty of Engineering and CENIDE. University of Duisburg-Essen, Carl-Benz-Straße 199, 47057 Duisburg, Germany.*

[7] *Trina Solar, No.2 Trina Road, Trina PV Industrial Park, Xinbei District, Changzhou, Jiangsu 213031, China*

[8] *Friedrich-Alexander University Erlangen-Nuremberg, Bavarian Center for Applied Energy Research (ZAE Bayern), Erlangen, Germany.*

* Correspondence should be addressed to:

César Omar Ramírez Quiroz
E-Mail: omar.quiroz@fau.de

Christoph J. Brabec
E-Mail: christoph.brabec@fau

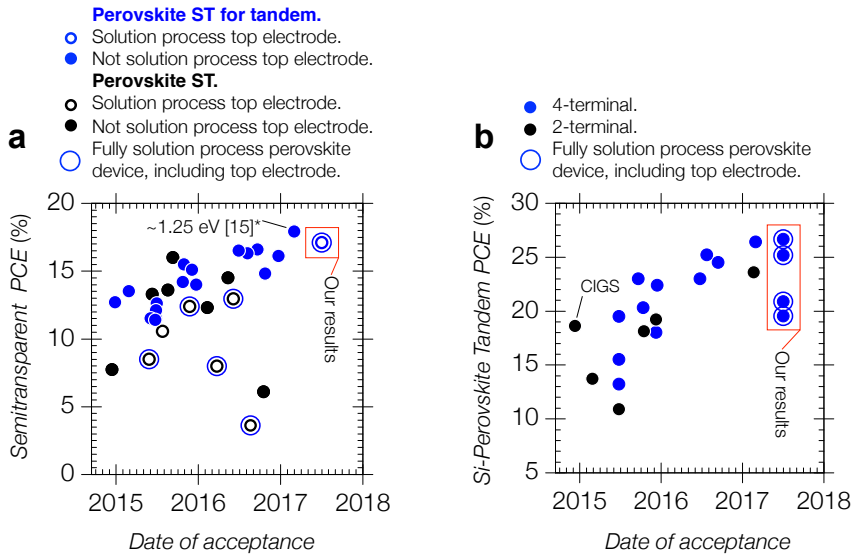

Figure S1. Recent progress for semitransparent (ST) perovskite photovoltaics (*1–15*), ST perovskite for tandem applications (*6*, *15–26*), as well as, silicon-perovskite tandem on its 4-terminal (*6*, *17*, *20–23*, *25–29*) and 2-terminal (*16*, *24*, *30*, *31*) modality. **a** shows reports on single junction semitransparent perovskite-based photovoltaics, and **b** shows the higher efficiency reported per study. In this review it is considered fully solution processed only when all the elements of the device architecture, except for one of the electrodes (e.g. ITO bottom electrode), are processed from solution to deliver the claimed efficiency. This definition is extended to antireflective coatings, electrodes, selective contacts and buffer layers. Unless stated otherwise, for **c** only perovskite-based tandem architectures coupled with silicon technologies are considered. * On the data point corresponding to [15] on the panel **a**, the reported semitransparent architecture utilizes a low-bandgap mixed tin-lead iodide perovskite absorber not suitable for Si-based multijunction applications.

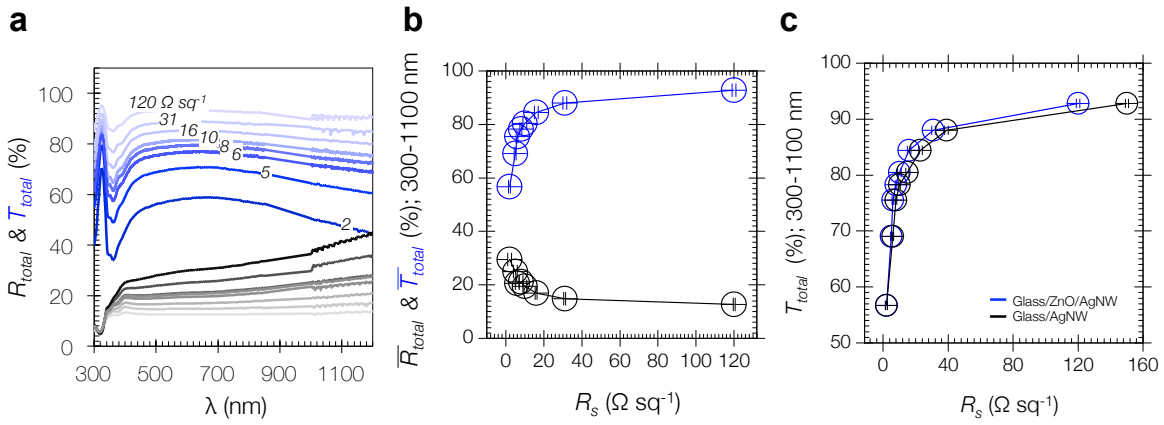

Figure S2. Total transmittance and reflectance spectra of AgNW layers with various sheet resistance deposited on glass, **a**. Average total transmittance and average total reflectance (300 nm to 1100 nm) as a function of sheet resistance (R_s) of the AgNW film deposited on glass, **b**. Total transmittance *vs* sheet resistance for AgNW layers on top of ZnO and on bare glass. In order to accurately measure the sheet resistance, for each AgNW layer thickness we deposited a control layer on top of ZnO to represent the relevant surface. Optical characterization was extracted from the films deposited on glass in order to disregard any optical effects from the ZnO, **c**.

Table S1. Key metrics for devices using AgNW top electrode with different sheet resistance.

Illumination conditions[a]	*AgNW sheet resistance*	*EQE/Sol. Sim. J_{sc} (mA cm^{-2})*	*PCE (%)*[b]	*Voc (V)*	*FF*	*S_{series} (Ω cm^2)*
G-illuminated	*120 Ωsq^{-1}AgNW*	7.59/8.56	**3.0**/3.3	0.93	0.42	715
W-illuminated		8.63/9.62	**3.4**/3.7	0.93	0.42	
	31 Ωsq^{-1}AgNW	11.56/12.52	**6.4**/6.6	0.95	0.55	361
		11.43/12.44	**6.0**/6.5	0.94	0.55	
	16 Ω^{-1}AgNW	12.25/13.15	**6.8**/7.1	0.95	0.57	229
		11.54/12.53	**6.2**/6.8	0.95	0.57	
	10 Ωsq^{-1}AgNW	13.09/14.02	**8.5**/8.6	0.94	0.65	110
		11.63/12.64	**7.1**/7.7	0.94	0.65	
	8 Ωsq^{-1}AgNW	13.35/14.25	**8.3**/8.9	0.93	0.67	89
		12.27/13.28	**7.6**/8.3	0.93	0.67	
	6 Ωsq^{-1}AgNW	14.23/15.29	**9.3**/10.0	0.95	0.69	88
		11.35/12.64	**7.4**/8.3	0.94	0.69	
	5 Ωsq^{-1}AgNW	15.49/16.52	**10.8**/11.6	1.00	0.70	71
		11.60/12.61	**8.1**/8.8	1.00	0.70	
	2 Ωsq^{-1}AgNW	16.41/17.46	**11.5**/12.3	0.99	0.72	78
		7.63/8.64	**5.3**/6.0	0.98	0.72	
	Ag evap.	16.65/17.64	**12.1**/12.8	0.97	0.75	19

[a] *W-illuminated*; illuminated from the AgNW electrode. *G-illuminated*; illuminated from the glass substrate.
[b] *PCE* values are calculated using short circuit photocurrent extracted from *EQE* characterization, and from the short circuit photocurrent extracted from *J-V* characterization AM 1.5 irradiation at 0.1 W/cm^2 illumination. * The values presented are averaged over a total of 12 cells per experimental variation.

Characterization of the electrode; bulk and percolative regimes

The bulk regime corresponding to the area with low sheet resistance can be expressed as:

$$T_{total} = \left[1 + \frac{Z_0}{2R_s}\frac{\sigma_{OP}}{\sigma_{DC}}\right]^{-2}, \qquad \text{(eq. S1)}$$

where $Z_0 = 373.76$ ohms, is the impedance of free space; σ_{OP} is the optical conductivity; and σ_{DC} is the direct current conductivity. Accordingly, bulk-like behavior on nanostructured transparent conductors can be characterized by σ_{OP}/σ_{DC} as the figure of merit (FOM). Further-

more, by adapting the reminiscent model for describing electrical percolation, Coleman *at al.* derived a model that closely describes the relation between transmittance and sheet resistance in the percolative regime. The model is as follows:

$$T_{total} = \left[1 + \frac{1}{\Pi}\left(\frac{Z_0}{2R_s}\right)^{1/(n+1)}\right]^{-2}, \qquad \Pi = 2\left[\frac{\sigma_{DC}/\sigma_{OP}}{(Z_0 t_{min}\sigma_{OP})^n}\right]^{-2} \qquad \text{(eq. S2)}$$

where Π is the percolative FOM, n is the percolation number, and t_{min} is the necessary thickness to reach the bulk conductivity value σ_{DC}. A detailed mathematical and theoretical description of the derivation of bulk-like regime and percolation regime can be found elsewhere(*32–34*)

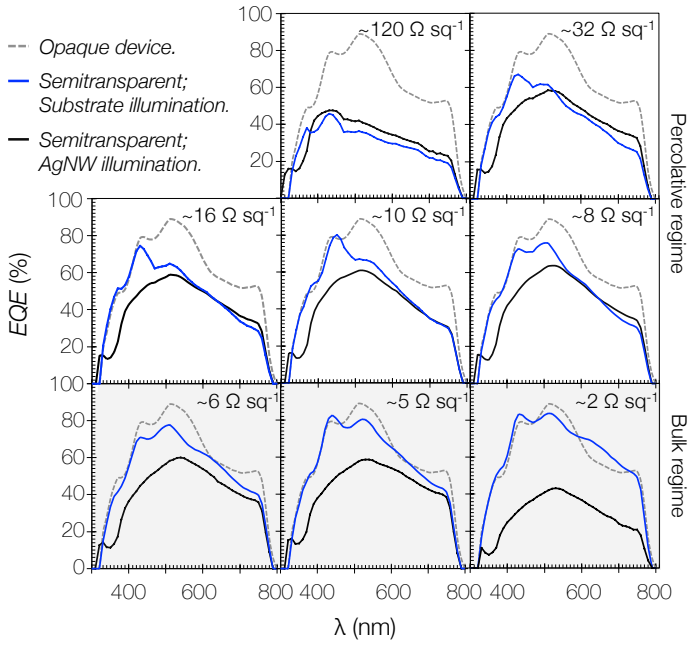

Figure S3. External quantum efficiency spectrogram analysis for devices with different illumination conditions on semitransparent devices.

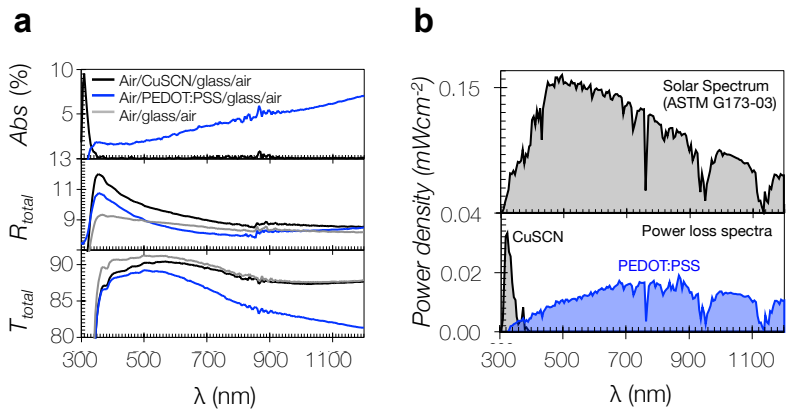

Figure S4. Total reflectance, total transmittance and absorption measurements of utilized selective contacts, **a**. In **b**, the upper panel shows the sun reference solar spectral irradiance AM1.5G 1 (ASTM G173-03), while the lower panel shows the power density spectra which is loss due to parasitic absorption. The power loss accounts for the simulated optical interference along with absorption contribution of the parasitic absorption.

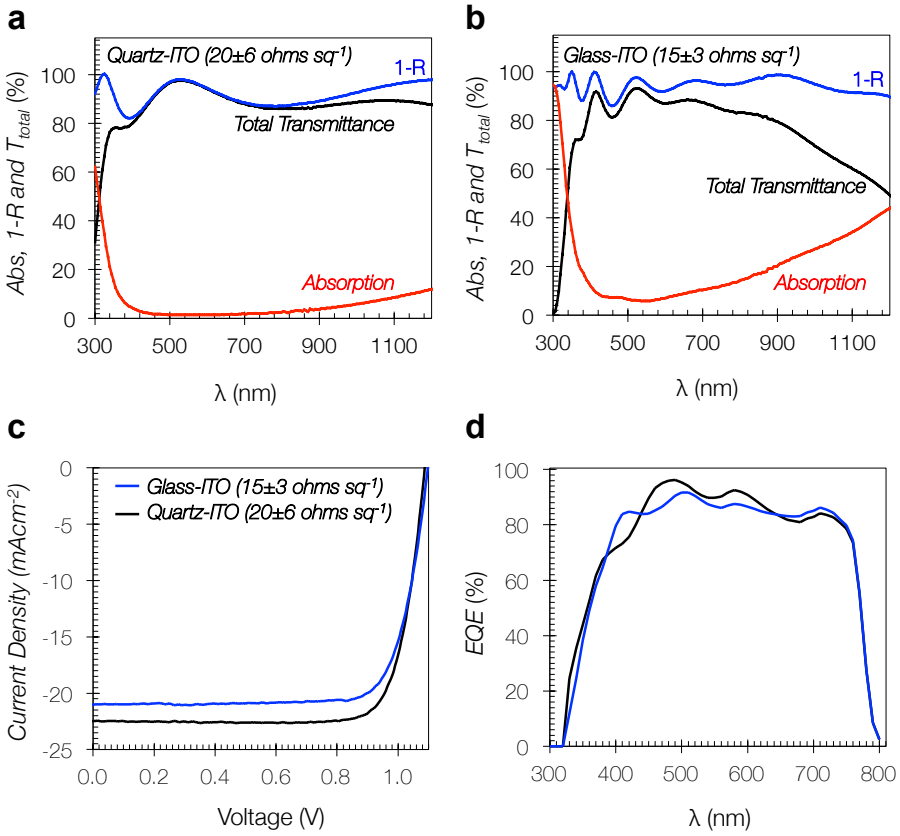

Figure S5. Optical properties comparison between the two different substrates; Quartz-ITO and Glass-ITO, **a** and **b**, respectively. Reflection and transmission spectra were corrected by the ITO/Air interface. **c** and **d** shows that the photovoltaic performance is not compromised whit the utilization of the quartz substrate.

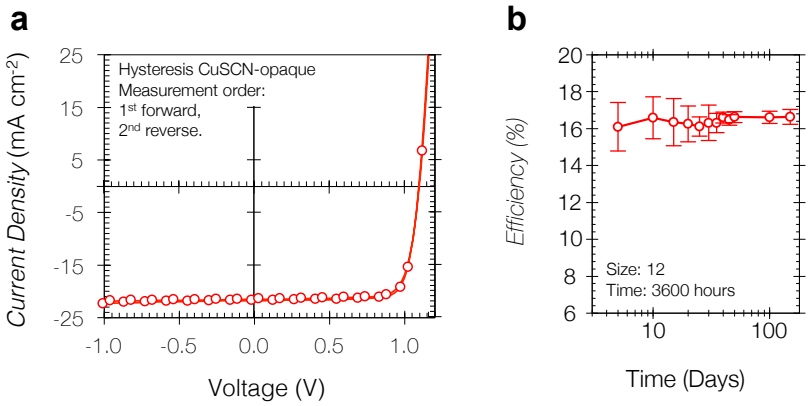

Figure S6. Hysteresis measurements of CuSCN-based opaque champion cell where the forward and consecutive reverse scan were extracted in same cycle, **a**. Efficiencies extracted from *J-V* characterization over a time lapse of 150 days while being stored in nitrogen atmosphere in the dark, **b**. Note that the efficiency of this devices performed within the error margin cited in the main text but do not reflect champion devices.

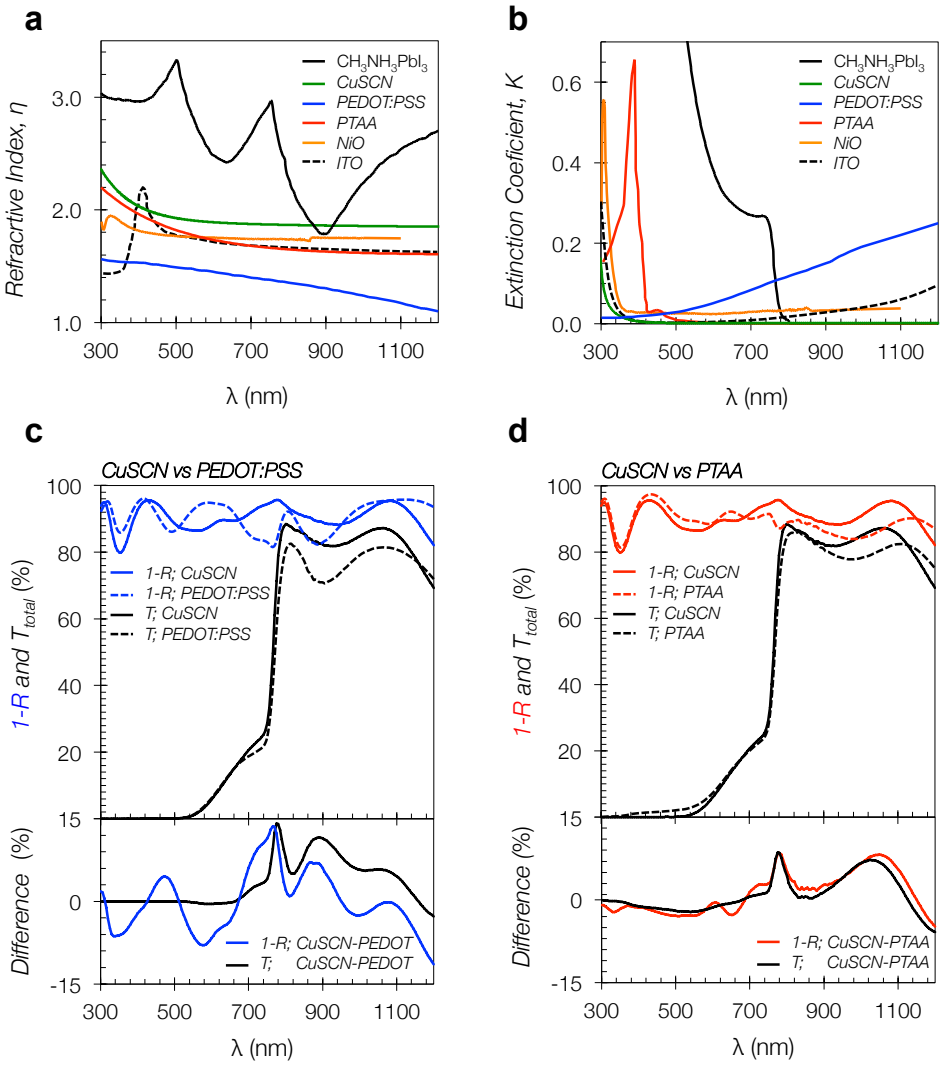

Figure S7. Optical constants for ITO, $CH_3NH_3PbI_3$, along with three different hole transporting materials commonly used in the literature and CuSCN, **a** and **b**. Transmittance and reflection profiles of PEDOT:PSS-based *vs* CuSCN-based full semitransparent devices showing that the difference on the transmittance profiles is not only due to reflection, **c**. Analogous PTAA *vs* CuSCN-based semitransparent devices showing that the difference on the reflection closely matches the difference in the transmittance, **d**.

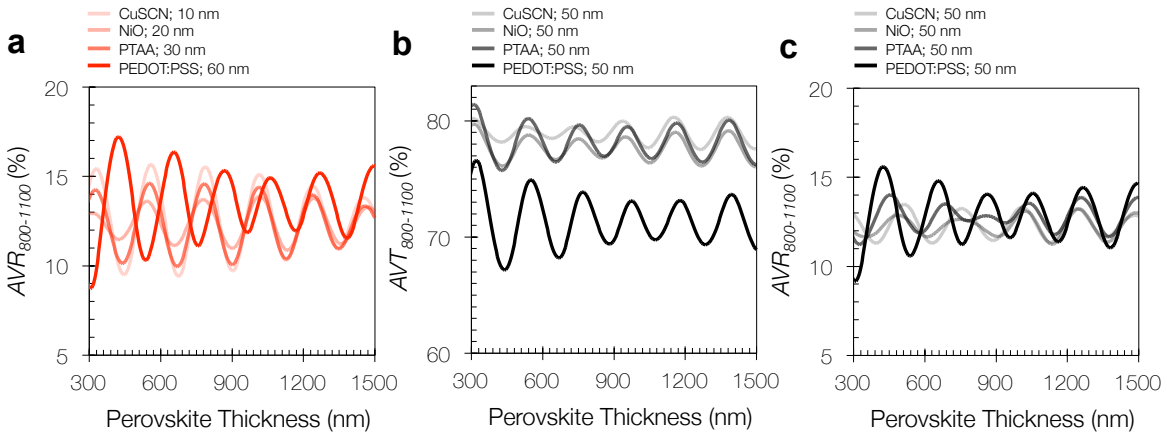

Figure S8. Simulated device average red transmittance (AVT; 800 nm to 1100 nm) for full perovskite semi-transparent cell stacks comprising various hole transporting layers (HTL). The thickness of the HTL layers is set constant at values reported from the literature while the thickness of the perovskite layer is varied**, a**. Same simulation with equally thick HTL, **b**. Corresponding simulated average reflectance (AVT; 800 nm to 1100 nm), **c**.

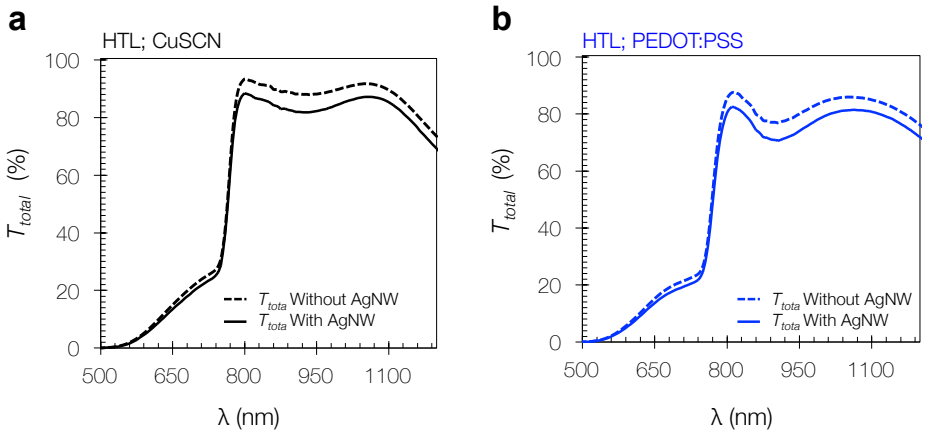

Figure S9. Total transmittance and reflectance for full device, including the electrode for the CuSCN-based semitransparent cell and the PEDOT:PSS- based semitransparent cell, **a** and **b**, respectively.

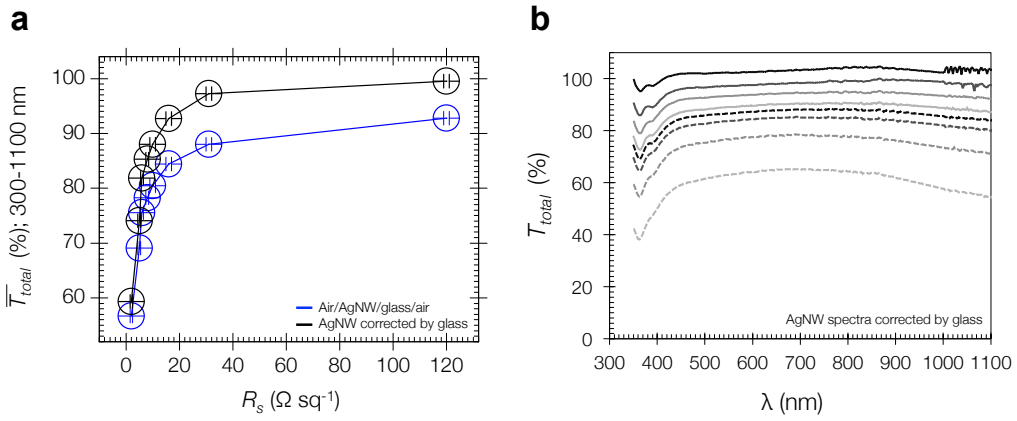

Figure S10. AgNW average total transmittance measurements corrected by contribution of underlying glass, **a,** and total transmittance spectra, **b**.

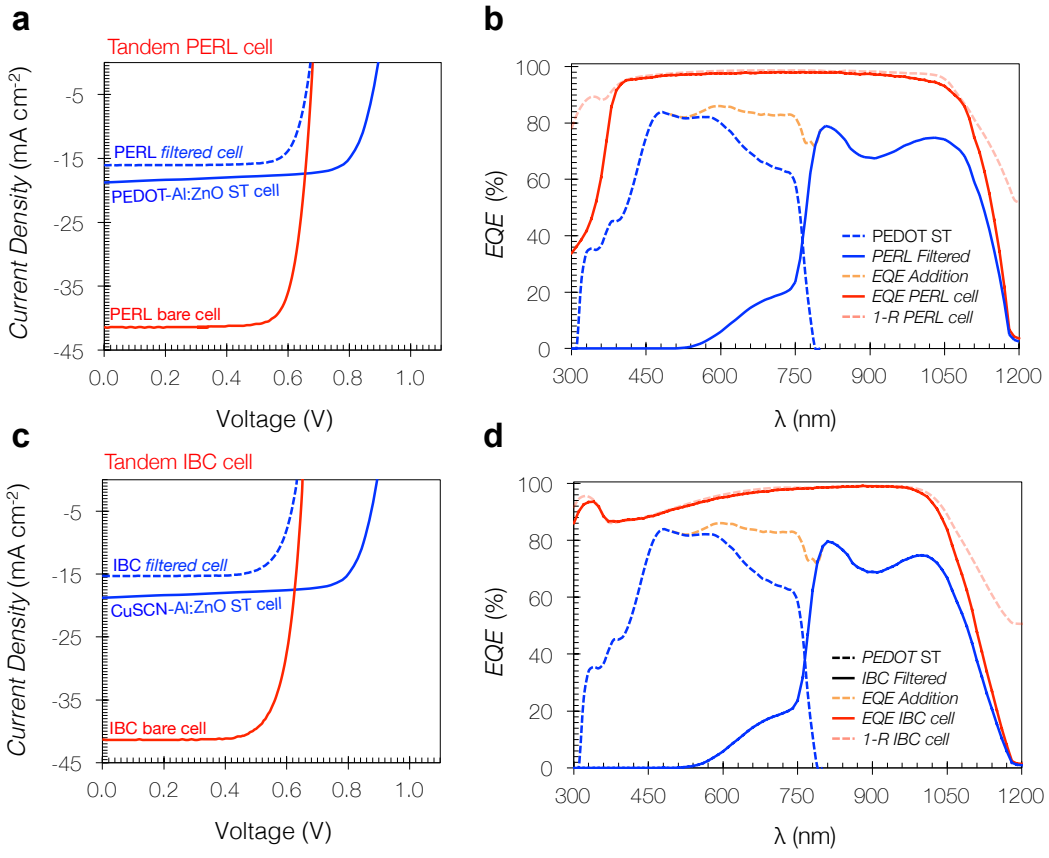

Figure S11. Representative photocurrent density-voltage curves under AM 1.5 irradiation at 0.1 Wcm^{-2} illumination, **a** and **c**. External quantum efficiency (*EQE*) spectrograms for PEDOT:PSS-based semitransparent perovskite along with silicon-bare cell and silicon-filtered by a semitransparent cell (including the electrode), PERL-based and IBC-based layouts **b** and **d**, respectively.

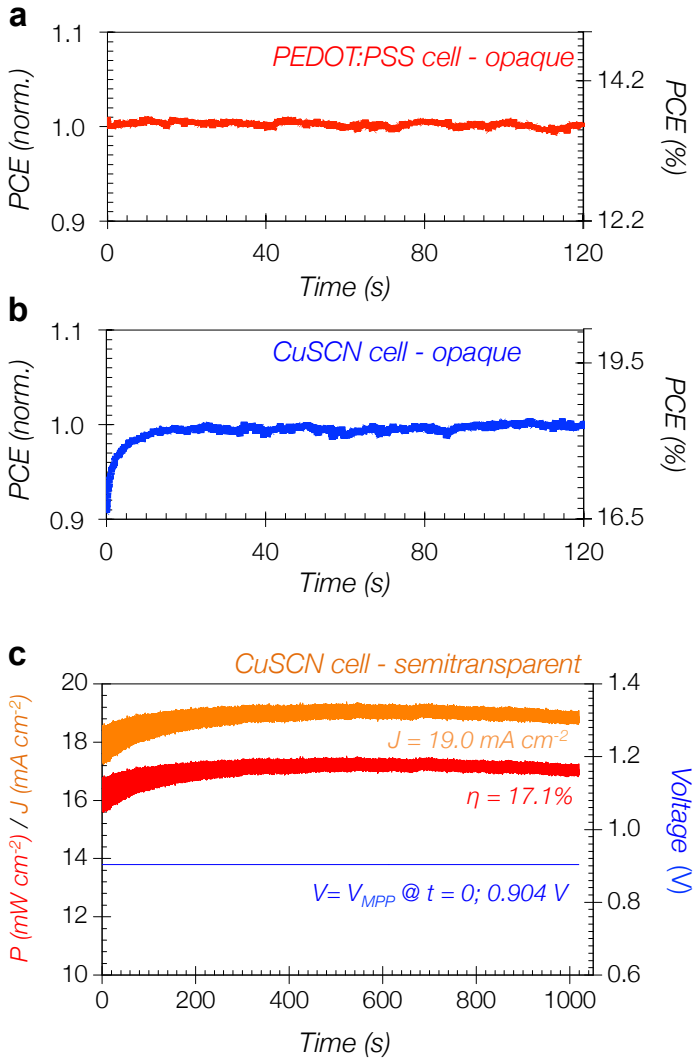

Figure S12. *Mpp* tracking response over time of both PEDOT:PSS and CuSCN-based opaque representative devices, **a** and **b**, respectively. Note that the device efficiency displayed on **a** and **b** performed within the error margin cited in the main text but do not reflect champion devices. **c**, Photovoltaic response of the semitransparent CuSCN-based device over time. After an initial IV measurement the cell was held at the initial V_{mpp} for the rest of the test. Measurements were performed with the solar cell mechanically stacked on top of a silicon cell and under a solar simulator emitting an AM 1.5G spectrum at 0.1 Wcm^2. *Mpp* tracking was performed with a Keithley 2400 source measure unit. After taking an initial full *JV* curve, the cell was held at the calculated V_{mpp}. Every second, a small voltage sweep with 5 data points in the range of V_{mpp} ± 20mV was recorded. The power output at each point was calculated and interpolated with a spline to find the precise new maximum power point. To avoid oscillations of the tracking algorithm, the bias voltage was not directly set to the new V_{mpp}, but a damping factor d was introduced so that $V_{bias} = V_{mpp}\ (previous) + d*[V_{mpp}\ (current) - V_{mpp}\ (previous)]$. The current was recorded continuously in between each tracking interval sampling 50 entries per second.

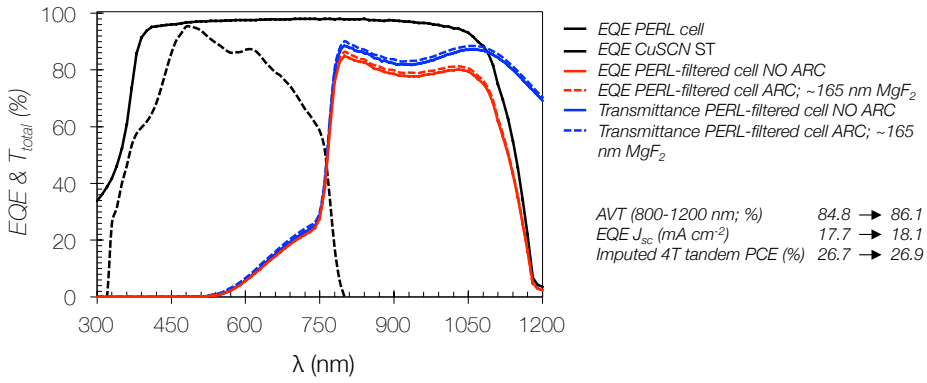

Figure S13. Effect of MgF_2 thermally evaporated on perovskite-based semitransparent solar cell (rear side of quartz substrate) on perovskite-tandem 4 terminal imputed efficiency. External quantum efficiency (*EQE*) spectrograms for semitransparent perovskite along with silicon-bare cell and silicon-filtered by a semitransparent cell (including the electrode).

Accelerated lifetime assessment of AgNW electrodes

Motivation: studying the optoelectronic performance of AgNW films under accelerated lifetime testing conditions.

Procedure: AgNW films doctor bladed on glass were kept a) under ~1 sun (metal halide lamp), b) in the dark under damp heat (85 °C/85%RH), c) in the dark (shelf test). All samples were kept in ambient air. Three samples per environment were probed periodically using UV/VIS absorption spectroscopy and 4-point probe.

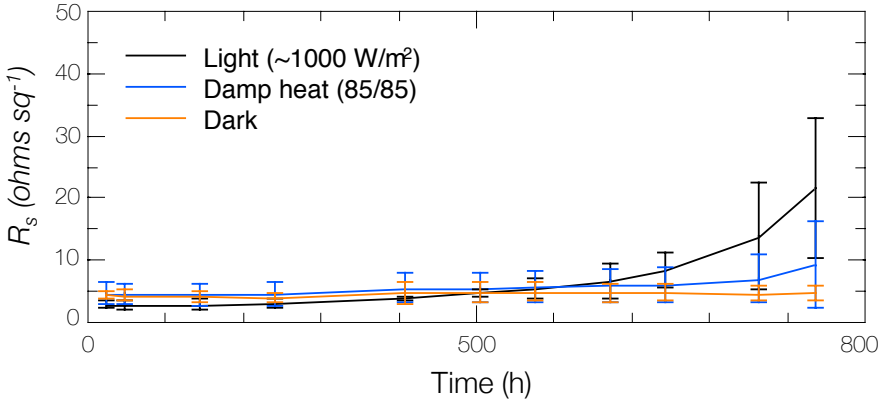

Figure S14. Sheet resistance of AgNW films over time under different conditions.

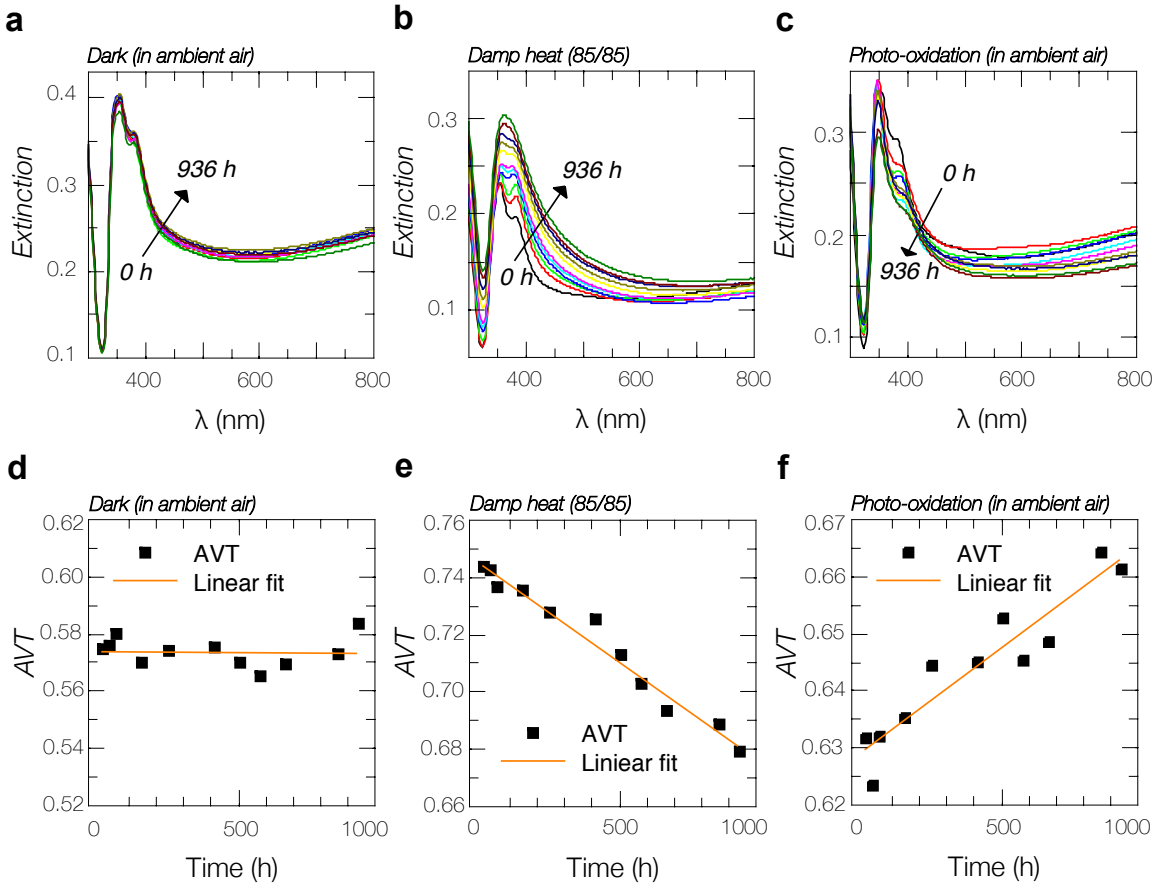

Figure S15. UV-Vis temporal behavior and average transmittance under: ~1 sun illumination (metal halide lamp) in air **c** and **f**; damp heat (85 ºC and 85% RH) **b** and **e**; and shelf-dark conditions in air **a** and **b**.

References

1. D. Bryant *et al*., A transparent conductive adhesive laminate electrode for high-efficiency organic-inorganic lead halide perovskite solar cells. *Adv. Mater.* **26**, 7499–7504 (2014).
2. K. A. Bush *et al*., Thermal and Environmental Stability of Semi-Transparent Perovskite Solar Cells for Tandems Enabled by a Solution-Processed Nanoparticle Buffer Layer and Sputtered ITO Electrode. *Adv. Mater.* **28**, 3937–3943 (2016).
3. Chih-Yu Chang, Kuan-Ting Lee, Wen-Kuan Huang, Hao-Yi Siao, Yu-Chia Chang, High-Performance, Air-Stable, Low-Temperature Processed Semitransparent Perovskite Solar Cells Enabled by Atomic Layer Deposition. *Chem. Mater.* **27**, 5122–5130 (2015).
4. E. Della Gaspera *et al*., Ultra-thin high efficiency semitransparent perovskite solar cells. *Nano Energy*. **13**, 249–257 (2015).
5. G. E. Eperon, V. M. Burlakov, A. Goriely, H. J. Snaith, Neutral color semitransparent microstructured perovskite solar cells. *ACS Nano*. **8**, 591–8 (2014).
6. F. Fu *et al*., Low-temperature-processed efficient semi-transparent planar perovskite solar cells for bifacial and tandem applications. *Nat. Commun.* **6**, 8932 (2015).
7. M. T. Hörantner *et al*., Shunt-Blocking Layers for Semitransparent Perovskite Solar Cells. *Adv. Mater. Interfaces*. **3**, 1–7 (2016).
8. J. Huang, G. Li, Y. Yang, A semi-transparent plastic solar cell fabricated by a lamination process. *Adv. Mater.* **20**, 415–419 (2008).
9. J. W. Jung, C.-C. Chueh, A. K.-Y. Jen, High-Performance Semitransparent Perovskite Solar Cells with 10% Power Conversion Efficiency and 25% Average Visible Transmittance Based on Transparent CuSCN as the Hole-Transporting Material. *Adv. Energy Mater.* **5**, 1500486 (2015).
10. C. O. Ramírez Quiroz *et al*., Coloring Semitransparent Perovskite Solar Cells via Dielectric Mirrors. *ACS Nano*. **49**, 1–5 (2016).
11. C. O. Ramírez Quiroz *et al*., Pushing Efficiency Limits for Semitransparent Perovskite Solar Cells. *J. Mater. Chem. A*. **3**, 24071–24081 (2015).
12. C. Roldán-Carmona *et al*., High efficiency single-junction semitransparent perovskite solar cells. *Energy Environ. Sci.* **7**, 2968 (2014).
13. K. Yang, F. Li, J. Zhang, C. P. Veeramalai, T. Guo, All-solution processed semi-transparent perovskite solar cells with silver nanowires electrode. *Nanotechnology*. **27**, 95202 (2016).
14. P. You, Z. Liu, Q. Tai, S. Liu, F. Yan, Efficient Semitransparent Perovskite Solar Cells with Graphene Electrodes. *Adv. Mater.* **27**, 3632–3638 (2015).
15. D. Zhao *et al*., Low-bandgap mixed tin–lead iodide perovskite absorbers with long carrier lifetimes for all-perovskite tandem solar cells. *Nat. Energy*. **2**, 17018 (2017).
16. C. D. Bailie *et al*., Semi-transparent perovskite solar cells for tandems with silicon and CIGS. *Energy Environ. Sci.* **8**, 956–963 (2014).
17. B. Chen *et al*., Efficient Semitransparent Perovskite Solar Cells for 23.0%-Efficiency Perovskite/Silicon Four-Terminal Tandem Cells. *Adv. Energy Mater.*, 1601128 (2016).
18. G. E. Eperon *et al*., Perovskite-perovskite tandem photovoltaics with ideal bandgaps. *Sci.* **9717**, 1–10 (2016).
19. F. Fu *et al*., High-efficiency Inverted Semi-transparent Planar Perovskite Solar Cells in Substrate Configuration. *Nat. Energy*. **2**, 1–27 (2016).
20. L. Kranz *et al*., *J. Phys. Chem. Lett.*, in press, doi:10.1021/acs.jpclett.5b01108.
21. F. Lang *et al*., Perovskite Solar Cells with Large-Area CVD-Graphene for Tandem Solar Cells. *J. Phys. Chem. Lett.* **6**, 2745–2750 (2015).

22. D. McMeekin, H. J. Snaith, A mixed-cation lead mixed-halide perovskite: The ideal absorber for tandem solar cells. *Sci*. **351**, 151–155 (2016).

23. J. Peng *et al*., Efficient Indium-Doped TiO x Electron Transport Layers for High-Performance Perovskite Solar Cells and Perovskite-Silicon Tandems. *Adv*. *Energy Mater*., 1601768 (2016).

24. T. Todorov *et al*., *Adv*. *Energy Mater*., in press, doi:10.1002/aenm.201500799.

25. J. Werner *et al*., *ACS energy Lett*., in press, doi:10.1021/acsenergylett.6b00254.

26. Y. M. Yang, Q. Chen, Y. Hsieh, T. Song, N. De Marco, Multilayer Transparent Top Electrode for Solution Processed Perovskite / Cu (In , Ga)(Se , S) 2 Four Terminal Tandem Solar Cells. *ACS Nano*. **9**, 7714–7721 (2015).

27. R. Sheng *et al*., Four-Terminal Tandem Solar Cells Using CH ₃ NH ₃ PbBr ₃ by Spectrum Splitting. *J*. *Phys*. *Chem*. *Lett*. **6**, 3931–3934 (2015).

28. K. A. Bush *et al*., Thermal and Environmental Stability of Semi-Transparent Perovskite Solar Cells for Tandems Enabled by a Sputtered ITO Electrode. *Adv*. *Mater*. *Submitt*., 1–7 (2015).

29. T. Duong *et al*., Rubidium Multication Perovskite with Optimized Bandgap for Perovskite- Silicon Tandem with over 26% Efficiency. *Adv*. *Energy Mater*. **1700228**, 1–11 (2017).

30. S. Albrecht *et al*., Monolithic Perovskite/Silicon-Heterojunction Tandem Solar Cells Processed at Low Temperature. *Energy Environ*. *Sci*. **9**, 81–88 (2015).

31. J. Werner *et al*., Efficient Monolithic Perovskite/Silicon Tandem Solar Cell with Cell Area >1 cm2. *J*. *Phys*. *Chem*. *Lett*. **7**, 161–166 (2016).

32. S. De, P. J. King, P. E. Lyons, U. Khan, J. N. Coleman, Size effects and the problem with percolation in nanostructured transparent conductors. *ACS Nano*. **4**, 7064–7072 (2010).

33. M. Dressel, G. Gruener, G. F. Bertsch, *Electrodynamics of Solids: Optical Properties of Electrons in Matter* (2002), vol. 70.

34. S. Sorel, P. E. Lyons, S. De, J. C. Dickerson, J. N. Coleman, The dependence of the optoelectrical properties of silver nanowire networks on nanowire length and diameter. *Nanotechnology*. **23**, 185201 (2012).